Astrophys Space Sci (2018) 363:92
https://doi.org/10.1007/s10509-018-3315-0

ORIGINAL ARTICLE

Super resolution for astronomical observations

Zhan Li[1,2,3] · Qingyu Peng[1,2] · Bir Bhanu[3] · Qingfeng Zhang[1,2] · Haifeng He[2]

Received: 1 November 2017 / Accepted: 31 March 2018

Abstract In order to obtain detailed information from multiple telescope observations a general blind super-resolution (SR) reconstruction approach for astronomical images is proposed in this paper. A pixel-reliability-based SR reconstruction algorithm is described and implemented, where the developed process incorporates flat field correction, automatic star searching and centering, iterative star matching, and sub-pixel image registration. Images captured by the 1-m telescope at Yunnan Observatory are used to test the proposed technique. The results of these experiments indicate that, following SR reconstruction, faint stars are more distinct, bright stars have sharper profiles, and the backgrounds have higher details; thus these results benefit from the high-precision star centering and image registration provided by the developed method. Application of the proposed approach not only provides more opportunities for new discoveries from astronomical image sequences, but will also contribute to enhancing the capabilities of most spatial or ground-based telescopes.

Keywords Methods: data analysis · Techniques: image processing · Telescopes · Stars: imaging

✉ Z. Li
lizhan@jnu.edu.cn

[1] Department of Computer Science, Jinan University, Guangzhou, China

[2] Sino-France Joint Laboratory for Astrometry, Dynamics and Space Science, Jinan University, Guangzhou, China

[3] Center for Research in Intelligent Systems, Department of Electrical and Computer Engineering, University of California, Riverside, USA

1 Introduction

Telescopes remain highly useful tools in the field of astronomical observation, facilitating important discoveries. However, higher resolutions for captured observations in charge-coupled device (CCD) frames using telescope imaging systems are desired, because the additional details provided in the resultant images would yield a higher probability of new discoveries. Additionally, most applications such as object detection, recognition, tracking, or high-precision positioning would benefit from higher-resolution observation frames. Telescopes with larger diameters produce higher-resolution CCD frames, but are also significantly more expensive to manufacture and maintain. An alternative solution to these problems is to improve the image resolutions using post-processing techniques.

The resolutions of astronomical observations are theoretically determined by the telescope diffraction limit (Wang et al. 2015). For ground-based systems, the angular resolutions are reduced significantly by atmospheric turbulence. However, near diffraction-limited images can be acquired under certain conditions using AO (Bennet et al. 2016) and LI (Cagigal et al. 2016; Law et al. 2006) methods, which can compensate for the atmospheric distortions. Further, resolution enhancement requires efforts to break the telescope diffraction barrier.

Super-resolution (SR) image reconstruction is a resolution enhancement process through which high-resolution (HR) images are produced from one or more low-resolution (LR) observed images (Park et al. 2003); this allows images to be recovered with a higher resolution than the diffraction limit (Neice 2010). Different from general deconvolution approaches to remove the blur indicated by the point spread function (PSF), or classic denoising techniques to improve signal-to-noise ratios (SNRs) for astronomical images, in SR reconstruction, several frames are mapped onto

Published online: 10 April 2018

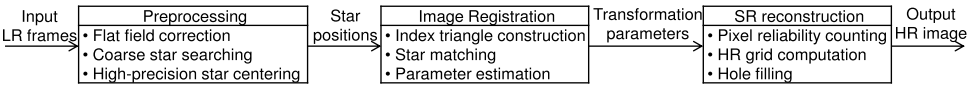

Fig. 1 SR reconstruction process for astronomical observations

one image. This approach is not employed to deblur or denoise, but rather as an image fusion method to re-compute the pixel values on an up-sampled scale. According to the Nyquist Sampling Theorem, the sinc-function can be used to perfectly reconstruct band-limited signals within half the sample rate, but cannot recover higher-frequency signals; this may cause problems as a result of aliasing (Stone et al. 2001). Therefore, a radical method of reconstructing details beyond the diffraction limit of an imaging system is to improve the sampling rate, which means more samples are acquired and more information is obtained from the original signals.

In summary, algorithms based on blind deconvolution or denoising may be used to reconstruct near-diffraction-limited images. In contrast, benefiting from more information from samples obtained in more than one observation, SR reconstruction provides opportunities to recover details beyond the diffraction limit. Note that, if necessary, general deconvolution or denoising methods can be applied before or after the SR process.

However, because of the great difference between observed frames captured by telescopes and image sequences acquired by common cameras, there exist considerable difficulties in applying SR technology to astronomical image processing. On one hand, popular image registration algorithms based on feature extraction and matching are not directly applicable to astronomical images; On the other hand, to obtain more details from a telescope-observed sequence, a feasible image fusion method is necessary, as required by most reconstruction-based SR techniques. However, the direct interpolations or averages used in combination algorithms for CCD frames cannot generally be applied without introducing additional blurring or information loss. Therefore, research on SR for astronomical observations remains in its infancy.

To acquire more of the details missing as a result of aliasing and to improve the resolution for astronomical observations performed using ground-based or space-based telescopes, a general blind SR reconstruction method based on pixel reliabilities is proposed in this paper. Further, an SR astronomical image reconstruction (SRAIR) system, which is a kind of fully automated and catalogue-independent software, including preprocessing, image registration, and SR reconstruction, is developed. Figure 1 shows the process of the proposed SR approach. Beginning with preprocessing, including flat field correction and coarse-to-fine star searching and centering, the sub-pixel positions of the stars in each observed LR frame are extracted. Then, for image registration between two CCD frames, the inter-frame transformation parameters are initially estimated through star-index-triangle construction and searching, and they are computed precisely using an iterative process of star matching and parameter estimation. Moreover, pixels in the LR frames are re-projected onto a unified HR grid according to the transformation parameters. Next, for SR reconstruction, the pixel reliabilities are defined and computed. Based on the reliability values, the pixel intensities in the HR grid are computed. Finally, those "holes" without corresponding LR pixels are filled based on their neighbors' reliabilities and intensities. Thus, a HR output image is reconstructed.

The remainder of this paper is organized as follows. In Sect. 2, related works are reviewed and our contributions are listed. Section 3 introduces the three processes incorporated in our SRAIR system as well as the proposed pixel-reliability-based SR approach. The results of validation experiments conducted using actual telescope observations are presented and discussed in Sect. 4. Finally, in Sect. 5, our work is summarized and general conclusions are drawn.

2 Related work and contributions

2.1 Related work

Although many challenges exist regarding the application of SR to astronomical observations, progressive achievements have been made in related research. For example, as an initial attempt to stack image sequences for tip-tilt correction, Christou (1991) proposed a simple shift-and-add algorithm that aligns the centers of images successively captured in a short exposure time and then adds them. Later, for linear reconstruction of an image from undersampled, dithered data, Fruchter and Hook (2002) developed a method having the versatility of shift-and-add while preserving the photometry and resolution. The subsequently developed astronomical image processing software MADmap (Cantalupo et al. 2010) that utilizes a maximum-likelihood method by overlapping and adding CCD frames to map cosmic microwave background (CMB) data. To satisfy the resolution requirements for astrophysical analysis, Renard et al. (2011) analyzed 11 regularization terms and multiple reconstruction-process parameters using a multi-aperture image reconstruction algorithm. Those researchers concluded that SR of astronomical images can be achieved with increasing performance through the minimal coverage of object function filling. Orieux et al. (2012) implemented SR reconstruction of maps for the Spectral and Photometric Imaging Receiver (SPIRE) instrument of the Herschel

observatory, based on a linear approach resulting from a quadratic-regularized criterion and numerical optimization tools. The results of their experiments show that the SR reconstruction algorithm consistently yields superior results to those of a standard processing tool employing a co-addition method.

In 2012, Jarrett et al. (2012) significantly improved the spatial resolution of the Wide-field Infrared Survey Explorer (WISE) imaging by creating new mosaics using a resampling kernel and a deconvolution technique known as the maximum correlation method (MCM). Additional SR reconstruction results for galaxies were published in their subsequent research (Jarrett et al. 2013). Later, Castellano et al. (2015) implemented variational super-resolution reconstruction of astronomical observations based on L1 and L2 regularizations and tested them on simulated Euclid satellite images. In the same year, Wang et al. (2015) presented a real-time, free of posterior data processing and incoherent SR telescope, that recovers higher local Fourier frequency components beyond the cut-off frequency of the objective lens. Obuchi et al. (2016) developed an approximation formula for the cross-validation error of a sparse linear regression, and tested their model on simulated black-hole image reconstruction on the event-horizon scale with SR.

These studies constitute significant attempts to apply SR technology to astronomy, which mostly targeted a specific problem and used simulated data or space telescope observations.

2.2 Contributions

Related to the work of the above mentioned studies, the primary contributions of the present paper are as follows:

1. Presentation of a feasible and general solution, which is incorporated in our SRAIR system, for high-precision image registration and blind SR reconstruction of astronomical observations without prior knowledge of the telescope imaging system or the degradation process;
2. A proposed definition of pixel reliability and its application to the SR reconstruction process;
3. Testing of the proposed SR method on actual observed CCD frames captured by the 1-m telescope at Yunnan Observatory, China.

3 SR astronomical image reconstruction

With the aim of obtaining further details from several LR observations, SR reconstruction involves the precise combination of information from different frames into a single output, to enhance the image resolution without introducing additional blurring. We implement the proposed SR solution in the proposed SRAIR system, which can be divided into three modules as shown in Fig. 1: preprocessing, image registration, and SR reconstruction. Each of these modules is described individually in the following.

3.1 Preprocessing

Preprocessing begins with a flat field correction for each CCD observation and a coarse-to-fine automatic star searching and centering procedure.

The four digital centering algorithms with sub-pixel precision most frequently used for star centroid detection are the modified moment (MM) (Stone 1989), median (MD) (Chiu 1977), derivative search (DS) (Stetson 1979), and Gaussian fitting (GF) (van Altena and Auer 1975; Auer and Van Altena 1978) algorithms. DS is especially efficient for images with crowded stars; however it is the least precise of the four methods (Stone 1989). MD is superior to DS, but slightly inferior to MM and GF in terms of precision. Benefiting from image-thresholding techniques, MM can obtain a centroid precision of the order of milli-arcseconds (Peng et al. 2008). Although GF typically fails with regard to the centering of weak stellar images with high background levels, it is frequently used to center well-sampled bright stars when high-precision centroid estimation is required. Based on actual CCD images taken by the 1-m telescope at Yunnan observatory, our previous work (Li et al. 2009) showed that the two-dimensional GF formulated in Eq. (1) with no threshold has the highest precision of the four considered methods.

$$G(x, y) = B + H \exp\left[-\frac{(x - x_i)^2 + (y - y_i)^2}{2\sigma^2}\right], \tag{1}$$

where (x_i, y_i) is the position of the i-th star center and B, H, and σ are the average intensity of the sky background, the intensity of star center (x_i, y_i), and the standard deviation of the Gaussian function, respectively. Further, the instrumental magnitude mag_i of the i-th star is computed from (Da Costa 1992)

$$mag_i = zpt - 2.5 \log\left(\sum_{(x-x_i)^2+(y-y_i)^2 \le r^2} P(x, y) - N_{pix} \times B\right), \tag{2}$$

where the zero point zpt is an arbitrary number to produce a reasonable output for the magnitudes; this parameter is set to 25 in our experiments as a typical value (Da Costa 1992). In addition, $P(x, y)$ is the intensity of the pixel located at (x, y), which is inside an aperture of radius r. N_{pix} is the number of pixels in the aperture. B is the average intensity of the sky background. In this equation, the magnitude is computed by a negative logarithmic function of the star flux in parentheses.

Combining the high efficiency of DS with the precision advantage of GF, an automatic star searching and centering technique is applied to each observed CCD frame in the proposed technique. For images containing dozens or hundreds of stars, DS is first used for rapid star searching and initial centering; then, two-dimensional GF is applied to compute the sub-pixel star situations with higher precision. As a result, all searched star centers (x_i, y_i) (supposing a total of m stars, i.e., $i = 1 - m$) are sorted by their magnitudes and recorded in terms of their pixel positions.

3.2 Image registration

To map pixels in several observed LR frames onto a unified HR grid, the relative geometric transformations between LR frames should be estimated with high precision. In the proposed method, we compute the transformation parameters of two matched images with sub-pixel precision based on the star positions and their matching relationships.

Different from star matching between an observed CCD image and a stellar catalogue in most other astronomical image registration routines, registration performed in this paper between two frames emphasizes precision above efficiency. This is because, on one hand, the number of searched stars in an image is considerably smaller than the stars in a stellar catalogue; thus, the efficiency difference is unimportant. On the other hand, for most multi-frame SR algorithms, registration precision directly and usually decisively influences the quality of the reconstructed image. Therefore, a triangle-based star matching technique (Tabur 2007) is implemented in this paper, so as to obtain an initial estimation of the transformation parameters. Then, an iterative process that alternately matches the star pairs and updates the parameters to improve the registration precision is used. In summary, first, any one of observations is selected as a reference image. Then, for the SR reconstruction from several images, SRAIR matches stars between two frames and aligns one other image to the reference image, but it does not carry out registration between an observed CCD image and a stellar catalogue. Therefore, SRAIR system is a kind of catalogue-independent software and it does not require the download of any catalogues.

As a result of the mechanical operation of the telescope tracking system and the shutter effect of the CCD array, small inter-frame translation, rotation and scaling effects may exist in an image sequence $\{LR_i\ (i = 0 - k)\}$ captured consecutively during a short period of time on one night. The affine transformation presented in Eq. (3), which covers all three geometric transformations, is frequently used to describe the relationship between the reference frame LR_0 and any other of these frames LR_i.

$$\begin{cases} x_0 = a_i x_i + b_i y_i + c_i \\ y_0 = d_i x_i + e_i y_i + f_i \end{cases} \quad i = 0, 1, 2, \ldots, k, \tag{3}$$

where (x_0, y_0) and (x_i, y_i) are the pixel coordinates in LR_0 and LR_i, respectively. For LR_0, $(a_i, b_i, c_i, d_i, e_i, f_i) = (1, 0, 0, 0, 1, 0)$. To estimate the six transformation parameters a–f, we require at least three pairs of matched star coordinates to obtain a unique solution from the equation. Therefore, a triangle-based matching algorithm, which uses stars to construct triangles and attempts to find a matched triangle pair between frames LR_0 and LR_i, is applied to obtain an initial estimation of parameters a_i–f_i for image LR_i.

The triangle-based algorithm first constructs index triangles via the centered stars in the images and then matches them by sorting and searching these triangles. Bright stars can be centered with a generally higher precision than faint stars. (In our experiments on ground-based observations Li et al. 2009, the position errors were less than 0.05 pixel for bright stars with magnitudes from 10 to 14, whereas they were 0.1–0.9 pixel for faint stars with magnitudes from 14.1 to 18.) Therefore, only n brighter stars are selected from m searched stars for index triangle construction. Generally, it is feasible and sufficient to choose 20–30 stars from each CCD frame for triangle construction (Tabur 2007).

For each triangle T, the ratio of the longest and shortest sides $T.Ratio$ and the cosine of the smallest angle $T.\cos\theta$ are computed. Their product $T.Ratio \times T.\cos\theta$ is then recorded as the index of this triangle (Tabur 2007). For convenient matching, all triangles constructed in an LR frame are sorted by their indices, and their vertices are recorded. Once a pair of triangles is found, the corresponding three star coordinates can be used to compute the initial values of a_i–f_i.

Generally, if a greater number of pairs of matched star coordinates can be used, a higher-precision parameter estimation can be obtained, as more information is used in the computation. We use parameters a_i–f_i to transform LR_i to LR_0 to find more matched star pairs, and use these matched star pairs to re-compute a_i–f_i. The least square method (LSM) is applied to solve Eq. (1). To improve the estimation precision, this iterative procedure alternately matches star pairs and updates the parameters until no further expansion of the set of matched star pairs occurs. The specific steps of the image registration process are listed in Fig. 2.

Although the registration routine is provided with this paper, it is to be noted that the SRAIR system allows for the inclusion of different pre-processing and registration steps, if these steps can lead to a high-precision estimation of the six affine transformation parameters a_i–f_i between frames at sub-pixel-precision as the SRAIR system does.

3.3 SR reconstruction

According to the inter-frame transformation parameters, pixels from several LR observations are mapped onto a refined HR grid. Next, to combine the information in multi-

ple LR frames into one output HR image, a pixel-reliability-based SR reconstruction method is proposed and applied.

First, to explain the concept of pixel reliability, we review the imaging process employed by a camera or astronomical imager. Figure 3 shows an image degradation model (Katsaggelos et al. 2007) relating the observed LR images to the desired HR image. SR reconstruction is an inverse problem to recover HR details from the LR sequence, which can be combined with deblurring and denoising techniques to improve the output image quality. It is assumed that the observed LR frames are down-sampled versions of the reconstructed HR image; thus, the LR image pixels are counterparts of the HR image pixels, and the SR reconstruction is a process of recovering the HR pixels from those in the LR images. Therefore, the greater the number of appearances of an HR pixel in the LR sequences, the more information on this pixel may be obtained, and the higher the reliability of the pixel intensity in the computation. In contrast, there are some pixels (referred to as "holes" here) in the HR image for which no counterpart can be found in any of the LR frames; therefore, we have no information on their intensities.

For a non-hole pixel, i.e., a "reliable" pixel, its reliability is defined as the number of times it appears in the LR sequence. This occurrence frequency can be computed by counting the points falling into the rectangular lattice representing this pixel after mapping. For a hole, however, the reliability is defined as a negative value, which is equivalent to the number of reliable pixels in its 3×3 neighborhood, subtracting 8. Figure 4 shows the pixel reliability matrix of the middle HR grid. First, a unified HR grid is constructed for the re-projection of different pixels from the LR_i frames. Then, each LR frame LR_i is mapped onto the grid according to its transformation parameters $a_i - f_i$. Subsequently, the pixel reliability matrix can be counted by considering the definitions of the pixel reliabilities.

It is important to compute the pixel intensities on the integer grid coordinates in the reconstructed HR image based on data on the non-integer positions of the points obtained from several different LR observations. Classical non-uniform interpolation algorithms calculate the HR pixels using traditional interpolating functions such as the nearest, bilinear, bi-cubic, and normalized sinc functions. However, these

Step 1. Define matching error bounds *epsRatio*, *epsCos* and *epsPoint* for *Ratio*, $cos\theta$, and star coordinates, respectively;

Step 2. For each triangle Ti_p in LR_i

2.1 find the nearest triangle $T0_q$ in LR_0 via a binary search of the products $T0_q.Ratio \times T0_q.cos\theta$;

2.2 if $|T0_q.Ratio - Ti_p.Ratio| < espRatio$ and $|T0_q.Cos\theta - Ti_p.Cos\theta| < espCos$, record the matched triangle pairs Ti_p and $T0_q$ and go to Step 4;

Step 3. Output "No matching triangles!";

Step 4. Compute initial estimates of a_i–f_i via vertex coordinates of matched triangles Ti_p and $T0_q$;

Step 5. Add three corresponding vertex pairs of Ti_p and $T0_q$ to matched star pair set S_{pairs};

Step 6. For each star coordinate pair (x_i, y_i) in LR_i

6.1 compute its corresponding coordinates (x'_i, y'_i) in LR_0 via eq. (1);

6.2 if $\|(x'_i, y'_i) - (x_0, y_0)\| < epsPoint$, add (x_i, y_i) and (x_0, y_0) to S_{pairs};

Step 7. If S_{pairs} is expanded, then compute a_i-f_i again using LSM according to S_{pairs} and go to Step 6;

Step 8. Output a_i–f_i.

Fig. 2 Triangle-match-based image registration algorithm

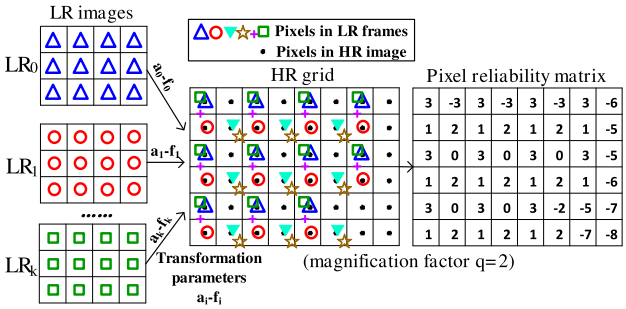

Fig. 4 HR grid and definition of pixel reliability

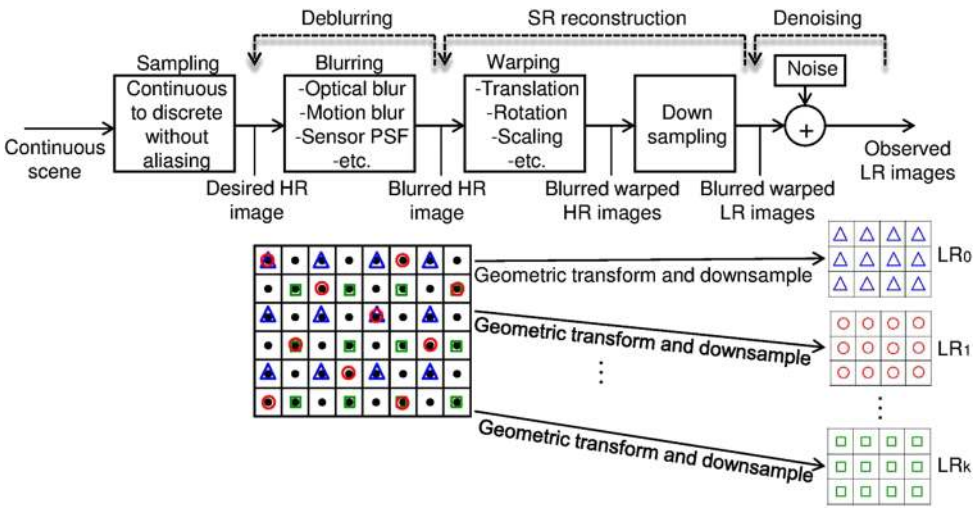

Fig. 3 Imaging degradation model relating LR images to HR images

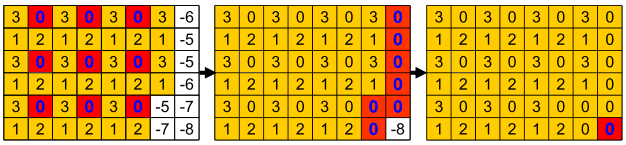

Fig. 5 Sequential hole filling according to reliabilities

methods ignore inevitable registration errors and cannot effectively handle the possible "holes" caused by insufficient LR frames or the high probability of pixel overlaps for mapping on the HR grid. The proposed pixel-reliability-based SR algorithm is tolerant of mapping errors within a $1/q$ (q is the magnification factor) pixel width for the LR images, as well as a high "hole" proportion larger than 70%.

In the proposed pixel-reliability-based SR approach, the HR pixel intensities can be computed based on their reliabilities. The intensities of non-hole pixels in the HR grid are assigned as the average intensities of the pixels mapped onto their rectangular lattices. The result of this average has zero dependence on the specific positions of any points in the lattice; therefore, the mapping errors may be limited to within one HR lattice without influencing the result. Thus, the proposed SR algorithm tolerates registration errors within one HR pixel. That is, if we reconstruct an image from the size $M \times N$ to size $qM \times qN$, a registration error within $1/q$ pixel width of the input images is allowed. This is achievable in our image registration process with sub-pixel-precision.

After all the intensities of the non-hole pixels are determined (we refer to this as "filling"), the holes are then filled by the weighted average of their reliable neighbors, the weights of which are their reliabilities. Thus,

$$P_{hole} = \sum_{i=1}^{8} w_i P_i / \sum_{i=1}^{8} w_i, \tag{4}$$

where P_{hole} and P_i are the pixel intensities of the center hole and its eight neighbor pixels in its 3×3 neighborhood, respectively, and w_i is the corresponding reliability of P_i for a non-hole pixel. Note that w_i is zero for a hole or an outside neighbor of an image boundary.

We use an iterative hole-filling strategy in the proposed SR algorithm, which divides holes into three levels according to their reliabilities: 0 to -3, -4 to -7, or -8, and fills holes in turn from 0 to -8 with three or more replicate scans, as shown in Fig. 5. After a hole has been filled (i.e., it has been assigned a value), its reliability is changed to 0 as a flag. Holes with reliabilities from 0 to -7 can be calculated from Eq. (4), because there exists at least one "reliable" pixel in their neighborhood providing some clues as to their values. However, if a hole has a reliability of -8, this means that none of its eight neighbors are available (because they are themselves "unfilled" holes or they are outside an image boundary). Therefore, they cannot be computed using Eq. (4) and should be left until some of their neighbors are assigned pixel intensities (as for the bottom-most right pixel in Fig. 5). The average intensities of their filled neighbors are assigned to these "deep" holes with reliabilities of -8. If they join together as blocks, we must fill them from the periphery to the center through several scans; however, this scenario rarely arises for an actual observed sequence. Frequently, an HR image will be reconstructed within 1 to 3 scans for "filling" holes even for a high "hole" proportion of 74% (with 6 frames used and $q = 4$).

Table 1 Specifications of telescope and CCD chip

Specifications	Parameters
Approximate focal length	1300 cm
F-ratio	13
Diameter of primary mirror	100 cm
CCD field of view	$6.4' \times 6.4'$
Pixel size	$24\mu \times 24\mu$
CCD array size	1024×1024
Angular extent per pixel	$0''.37$/pixel

4 Experimental results

4.1 Dataset

Although aligning and stacking techniques for astronomical observations have been studied for several years, most previous work has focused on improving the SNR or handling under-sampled images for simulated data or sequences captured by space telescopes (Fruchter and Hook 2002; Renard et al. 2011; Castellano et al. 2015; Obuchi et al. 2016). In this study, we used actual ground-based observations performed using the 1-m telescope at the Yunnan Observatory. The experiment was conducted on an image sequence of 18 frames observed on the night of January 2nd, 2004, with a 70-s exposure time and a zenith distance of 10–30 degrees. The specifications of the telescope and its attached CCD chip are listed in Table 1.

In fact, we tested our algorithm on actual image sequences observed from 2004 to 2016. For almost all these observed sequences, the proposed SRAIR system produced preferable resolution enhancement results compared to other systems mentioned in Sect. 4.4. The dataset presented in this paper is one of the typical tested sequences among them.

4.2 Performance metrics

The proposed SR reconstruction solution for astronomical observations is integrated in the SRAIR system, which was developed and tested in the MATLAB R2015a and Microsoft Visual Studio VC++6.0 environments.

To evaluate the performance of the proposed approach, three commonly used indexes for image quality evaluation were computed in our experiments.

4.2.1 Root mean square (RMS) contrast

The root mean square (RMS) contrast is defined as the standard deviation of the pixel intensities (Peli 1990) and can be computed according to

$$RMS = \sqrt{\frac{1}{n_1 \times n_2} \sum_{i=1}^{n_1} \sum_{j=1}^{n_2} (I_{ij} - \overline{I})^2}, \tag{5}$$

where the intensities I_{ij} are the i-th j-th element of the two-dimensional image of size n_1 by n_2. Generally, a larger image contrast yields greater object distinguishability.

4.2.2 Image entropy

The Shannon entropy (Shannon 1948) defined in Eq. (6) is often used for image assessment, to indicate the amount of information contained in an image (Gu et al. 2016). High-entropy images usually have larger contrast and contain more detail. Moreover, the entropy of a focused image is generally larger than that of an unfocused image (Thum 1984).

$$Entropy = -\sum_{k=1}^{K} p_k \log_2(p_k), \tag{6}$$

where K is the grayscale number (for a 16-bit FITS image, $K = 65535$), p_k is the probability of gray level k, and $\log_2$ is the base 2 logarithm.

4.2.3 Full width at half maximum (FWHM)

For astronomical observations, the full width at half maximum (FWHM) is a measure of the observation conditions. A smaller FWHM value corresponds to a sharper Gaussian profile and less blurring of astronomical objects such as stars. For a normal distribution $N(x_0, \sigma)$, the FWHM shown in Fig. 6 is related to the standard deviation σ by Eq. (7) (Stone 1989). The value of σ can be estimated by fitting the star profile to the two-dimensional Gaussian distribution formulated using Eq. (1).

$$FWHM = 2\sqrt{2 \ln 2}\sigma \approx 2.355\sigma. \tag{7}$$

4.3 Experimental results

4.3.1 Automatic star searching and centering

To evaluate the star position precision, we searched all 18 frames in a sequence, although only eight among them were used for the image registration and SR reconstruction. Figure 7 shows the results of the star searching and centering for the reference image of eight used frames. For this frame, 112 stars were initially searched using DS. Then, 87 among them were centered using GF; they are marked by green squares and numbered in yellow in the right image of Fig. 7.

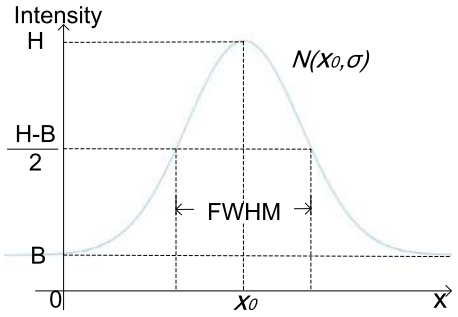

Fig. 6 FWHM of normal distribution $N(x_0, \sigma)$ of star profile. B, x_0, and H indicate the average intensity of the background, the center position of the star, and the intensity of the star center, respectively

Among these 87 centered stars, 70 common stars in all 18 frames with magnitudes from 10.2 to 17.6 were chosen to evaluate the average errors in the star positions. Figure 8 relates the average centering errors of the 70 stars to their magnitudes. The errors in both the x and y directions of all these stars have a precision of within 0.5 pixel. In particular, the error is 0.2 pixel for the 50 brightest stars (magnitudes < 16). Thus, the required sub-pixel star centering precision was achieved for high-precision image registration.

4.3.2 Star matching and image registration

The brightest 20 stars were used to construct the index triangles for each frame. Then, all centered stars were matched between the reference frame and each of the other frames shown in Fig. 9. The inter-frame transformation parameters were calculated according to the coordinates of the matched star positions and recorded in a log file.

4.3.3 SR reconstruction

Although the number of input images can be assigned to any positive integers, it doesn't mean that the higher the number of input images, the better the quality of the output. Due to different seeing conditions and various SNR degrees caused by atmospheric turbulence during the observation, as well as other complicated factors leading the image degradation, fusion of too many images may degrade the reconstructed output instead, let alone the significantly decreasing of system performance and efficiency accompanying with the increasing number of input image frames. Considering the computation complexity and an acceptable output result, only eight

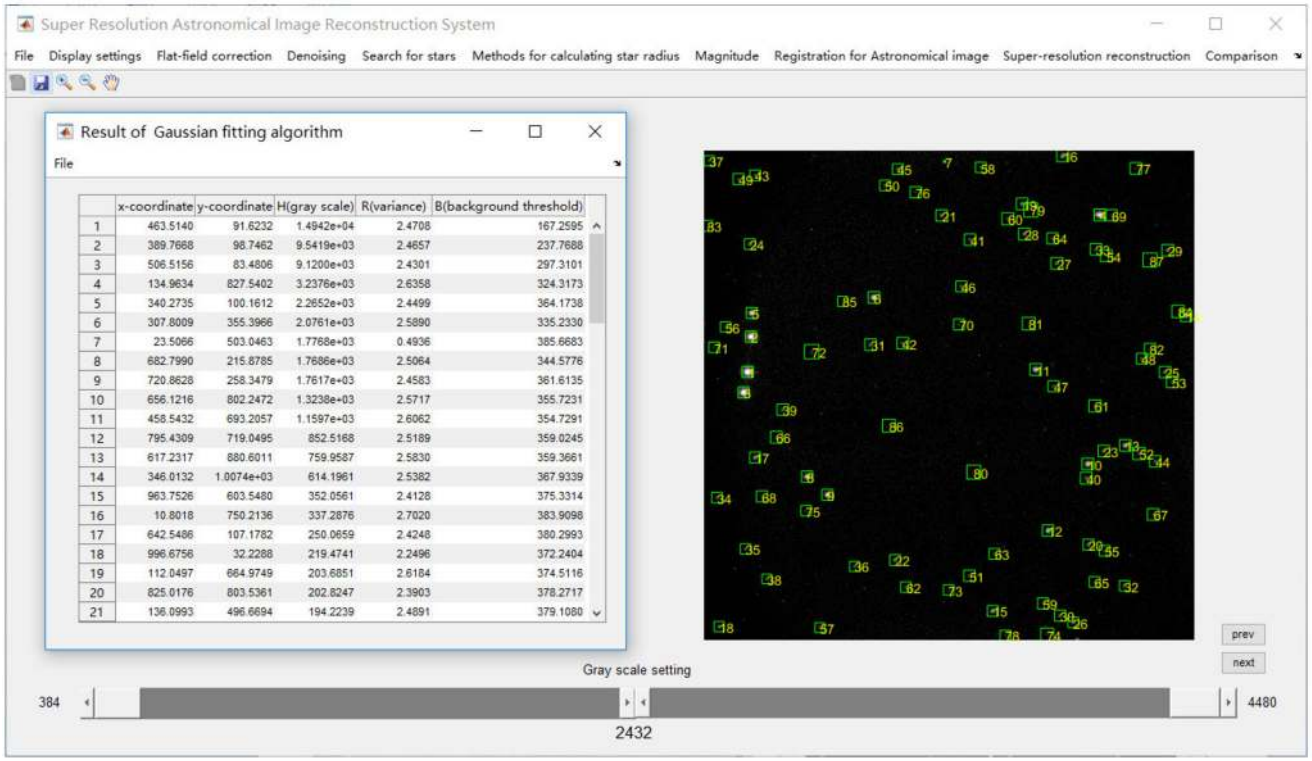

Fig. 7 Automatic star searching and centering for reference image. The searched stars are marked by green squares and numbered in yellow in the right sub-window with their position parameters listed in the left window

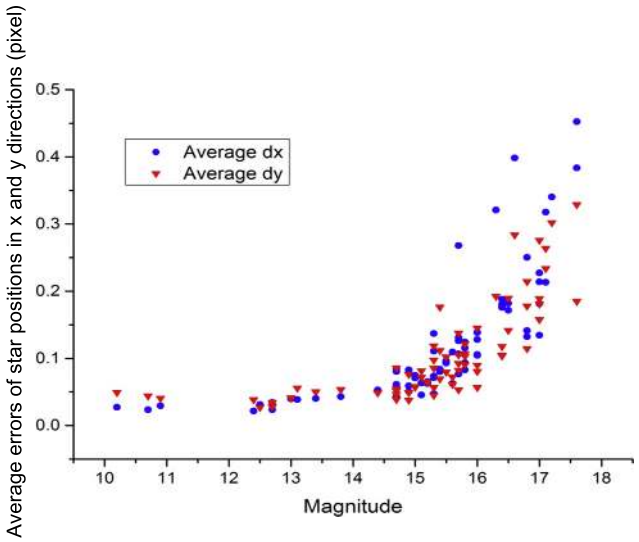

Fig. 8 Average position errors of 18 frames for 70 centered stars

frames from the 18 observations with similar seeing condition and comparable SNR degrees were used for the SR reconstruction. The results of the SR reconstruction and several other methods are displayed in Fig. 10 (the magnification factor $q = 2$). Four local areas numbered in the squares were magnified; their 3D maps are shown below. For better display on the screen, these areas are shown with grayscale stretching according to their local grayscale ranges. However, this presentation does not correspond to any changes in the pixel intensities of the output FITS images.

Note that the magnification factor q is the only parameter to be assigned by SRAIR users at the SR step. By a magnification factor q, input images with the resolution $M \times N$ will be SR reconstructed to the resolution $qM \times qN$. Theoretically, q can be assigned to any integers larger than 1 according to the user's specific needs. However, larger value of q requires more information from the input sequence which means higher numbers of input images, or otherwise higher "hole" proportions which will degrade the performance and efficiency of the system. We tested q from 2 to 6 in our experiments. If $q = 6$, SR reconstruction of a two-star local area of the size 40×40 to the output size 240×240 requires 5–7 seconds on a common personal notebook with Intel double i7 CPU 2.70 GHz 2.70 GHz, a memory of 16 GB RAM and the 64 bit Windows 10. On the other hand, experiments show that by using the iterative "hole-filling" strategy, the SRAIR system can well process a high "hole" proportion of 74% (with 6 frames used for $q = 4$). In sum, in the SRAIR system, to get acceptable outputs and efficiency, q is recommended to be set in the range of 2 to 4.

To further illustrate the significant difference between the proposed SR approach and classical interpolation al-

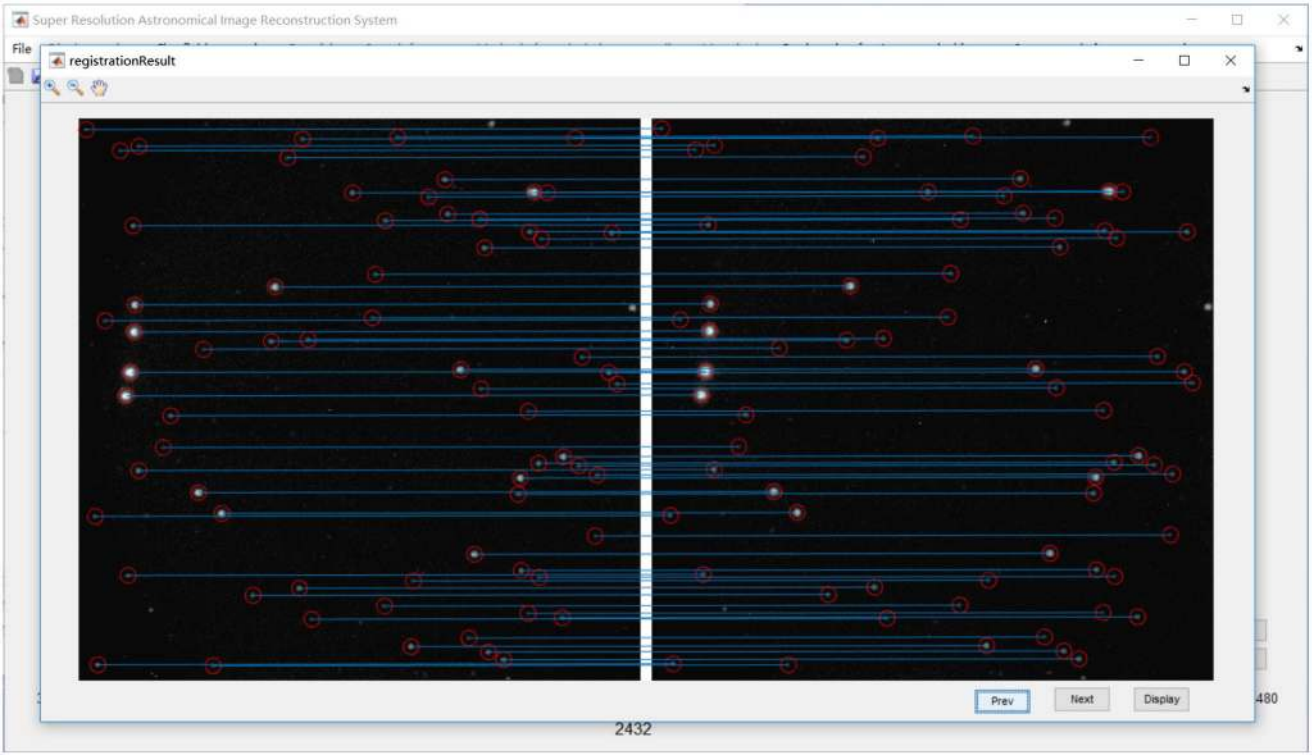

Fig. 9 Star matching and image registration. The searched stars are circled in red for each frame and matched in with blue lines between the reference frame and each frame in the sequence

gorithms or traditional aligning and stacking techniques, Fig. 11 shows an output comparison. The seven images in the top row are the same local areas clipped from an observed sequence recorded in 16-bit flexible image transport system (FITS) format (intensity range: 0–65535). Some white points are apparent in Frames 1, 3, and 6, which may indicate cosmic rays. The middle row displays the outputs of various methods (the identifying labels are at the column bottoms). To better show the differences, the local areas within the yellow boxes are magnified and their corresponding three-dimensional (3D) intensity maps are displayed in the bottom row. Figures 11(a) and 11(b) are traditional interpolations of Frame 1, which is viewed as the reference frame. As only Frame 1 is used, the details in the other frames, such as the white points in Frame 3 and 6, cannot be displayed. Interpolation techniques cannot essentially improve the resolution of an image without access to additional information beyond that provided by the image. On the other hand, to obtain details from different observations, classical weighted average or drizzle techniques (Fruchter and Hook 2002) used by the AstroimageJ (AIJ) (Collins et al. 2017) and DeepSkyStacker (DSS) (Gallaway 2016; German et al. 2005) systems combine multiple input frames into a single image through selection, alignment, and stacking (Figs. 11(c)–(e)). The white points in Frame 1, 3, and 6 are all indicated in Figs. 11(c)–(f). Among these outputs, AstroimageJ introduces obvious blurring apparent in Fig. 11(c), while our SRAIR system (Fig. 11(f)) produces sharper white points and finer backgrounds than the results obtained using the two DSS methods (Figs. 11(d) and 11(e)). Further, the 3D maps in the bottom row indicate that only the SRAIR system preserves the original intensity values from the input frames without introducing smoothness or intensity loss, as the pixel intensities of the input frames in this local area vary from 362 to 1161. To summarize, SR reconstruction techniques differ considerably from traditional aligning and stacking methods for resolution enhancement, as more details are reconstructed from different observations and the original input information is preserved.

4.4 Comparison

Seven methods were compared in our experiments, i.e., nearest interpolation (Nearest), normalized sinc function interpolation (Normalized Sinc), register and average (Regave), the stacking and combining used in the AstroimageJ System (AstroimageJ) (Collins et al. 2017), the two Drizzle methods (Fruchter and Hook 2002) used in the DeepSkyStacker System (DSS Mean Gallaway 2016 and DSS Entropy German et al. 2005), and the proposed SR solution (SRAIR).

The results of four local areas magnified by these seven methods are shown in Fig. 10. No. 1 is an area with a faint star and several white points due to cosmic rays or noise. No. 2 is an area with three faint stars and one white point.

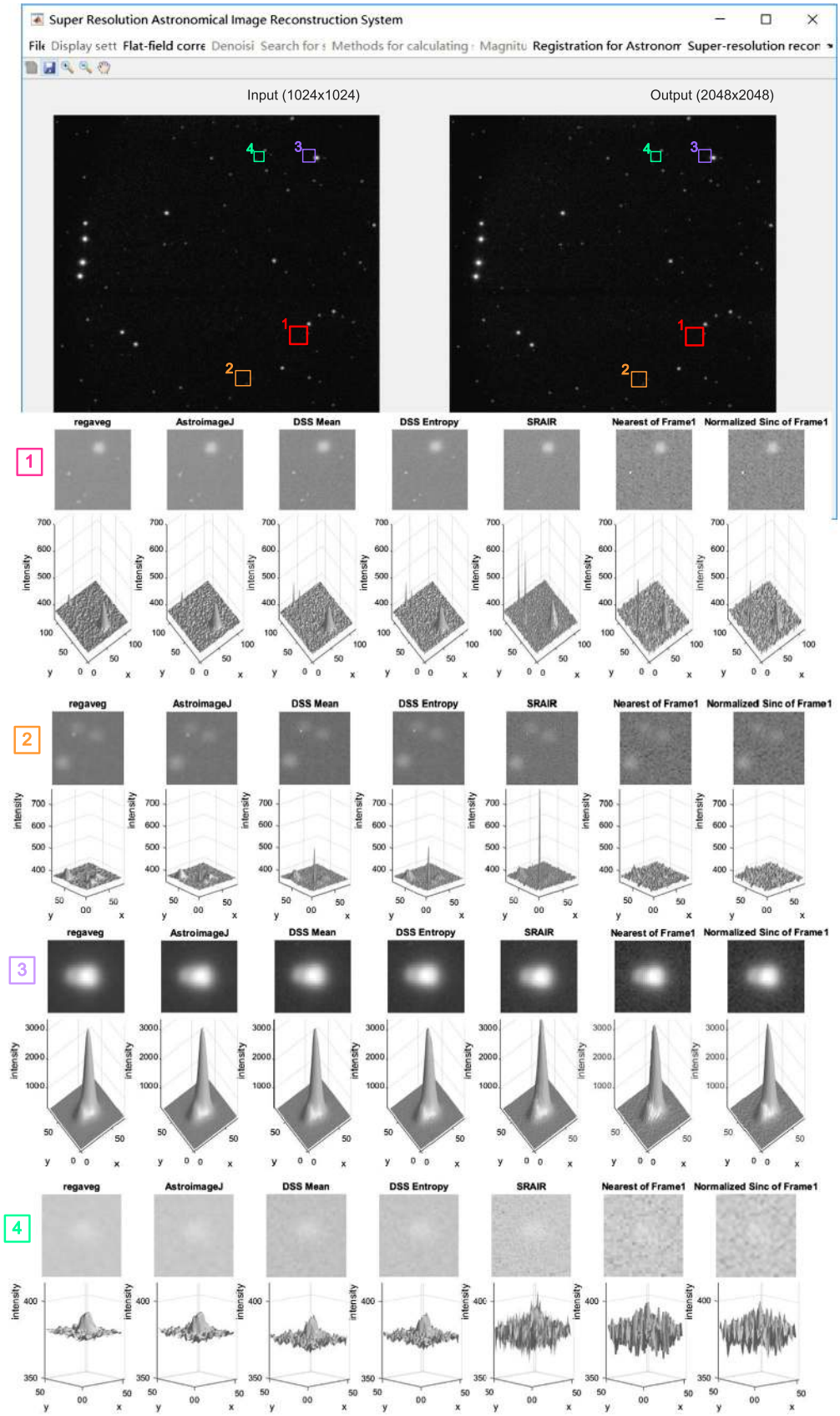

Fig. 10 SR reconstruction. Four local areas are magnified (with their 3D maps shown beneath) for better comparison of the different outputs. The input frames have sizes of 1024×1024. After twofold magnification, the output image size is 2048×2048 (i.e., $q = 2$)

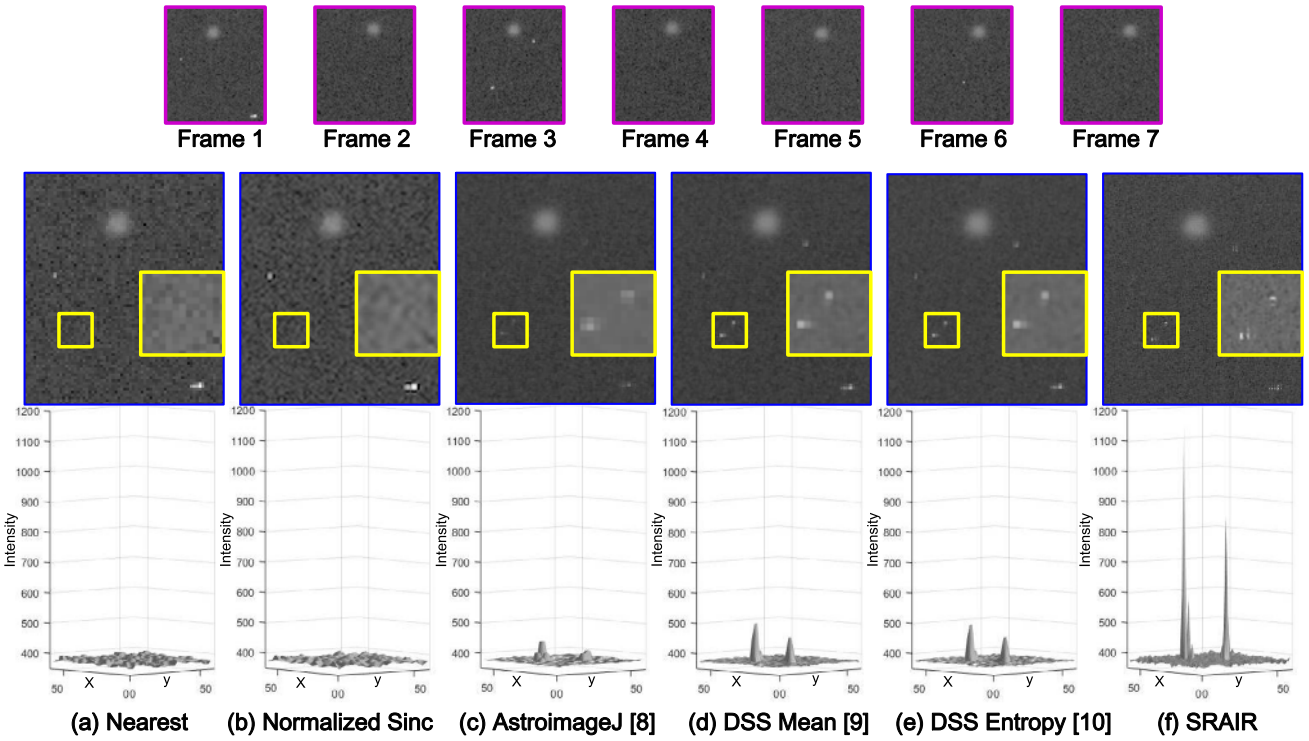

Fig. 11 Comparison of output images from different techniques. Top row: Seven input frames, where Frame 1 is the reference frame. Middle row: Twofold-magnified results of different methods. The local areas, which contain two white points from Frames 3 and 6, are magnified and contrast stretched by a unified scale in the yellow boxes. Bottom row: Intensity 3D maps of local areas in yellow boxes (for 16-bit FITS image, pixel intensity range: 0–65535)

No. 3 is an area with a bright star and a faint star close together. No. 4 is a faint star and there is extremely low SNR; the star can barely be distinguished from the background in the input frames. As for the visual effects, the two interpolation algorithms expand the image size from the reference image, but cannot reconstruct details from multiple inputs in one image; the white points in areas No. 1 and 2 from the non-reference frames are not shown in the output. Thus, these methods cannot radically improve the image resolution. The Reg-ave and AstroimageJ methods decrease the noise by stacking and averaging several frames, but inevitably add blur to the images and smooth the image details. The DSS Mean and DSS Entropy approaches have better outputs than the Reg-ave and AstroimageJ in terms of detail preservation. This is achieved by using Drizzle for stacking. However, severe information losses on the pixel intensities still occur; the intensity decreases for the white points in areas No. 1 and 2, and the smoothness for the faint star in the area No. 4. As SR combines samples from each LR observation, white points recorded in any of the other frames are displayed in the output of the SRAIR result. Moreover, sharper profiles are clearly apparent for the white points and finer backgrounds in the 3D maps of Fig. 10(e) compared to those of Figs. 10(a)–(d), in which blurring and smoothness are introduced. Relatively speaking, the SRAIR approach reconstructs the image at a higher resolution level and preserves more details from original input sequence with the least degree of information loss.

Preferable outputs using the proposed SR method can also be observed in Figs. 12 and 13, which display section curves in the x and y directions of area No. 3 (with a faint star near a bright star) and area No. 4 (with an extremely faint star) in Fig. 10. In Fig. 12, the SRAIR system produces a sharper Gaussian profile for the bright star than the others, as well as a slightly larger fluctuation caused by the faint star. In Fig. 13, as the intensities of this star area are very close to the background, all curves are influenced significantly by the noise. Among these curves, the SRAIR result retains the richest details from the original frames (which may be represented by two interpolation methods), while the other four combining methods obviously smooth the fluctuations.

To quantitatively evaluate the performance of the proposed SR solution, the three indexes, i.e., RMS contrast, entropy and FWHM, defined by Eqs. (4)–(6) in Sect. 4.2 were used for comparison. Five methods for stacking and combining astronomical sequences were compared, namely, Reg-ave, AstroimageJ, DSS Mean, DSS Entropy, and SRAIR.

We chose 58 stars with magnitudes of 10–18 among the 87 automatically searched stars. The other 29 stars were

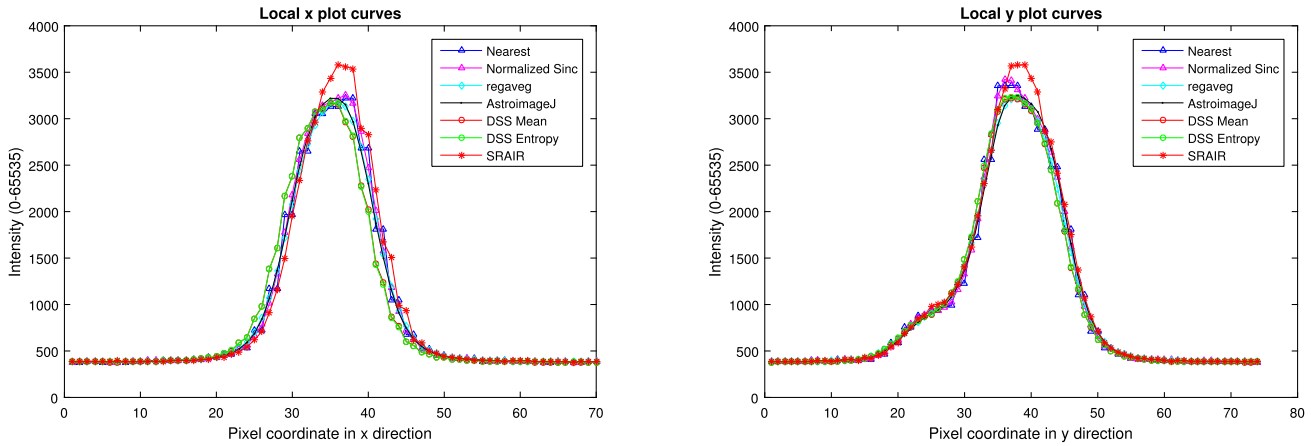

Fig. 12 Section curves in x and y directions on the intensity peak in area No. 3

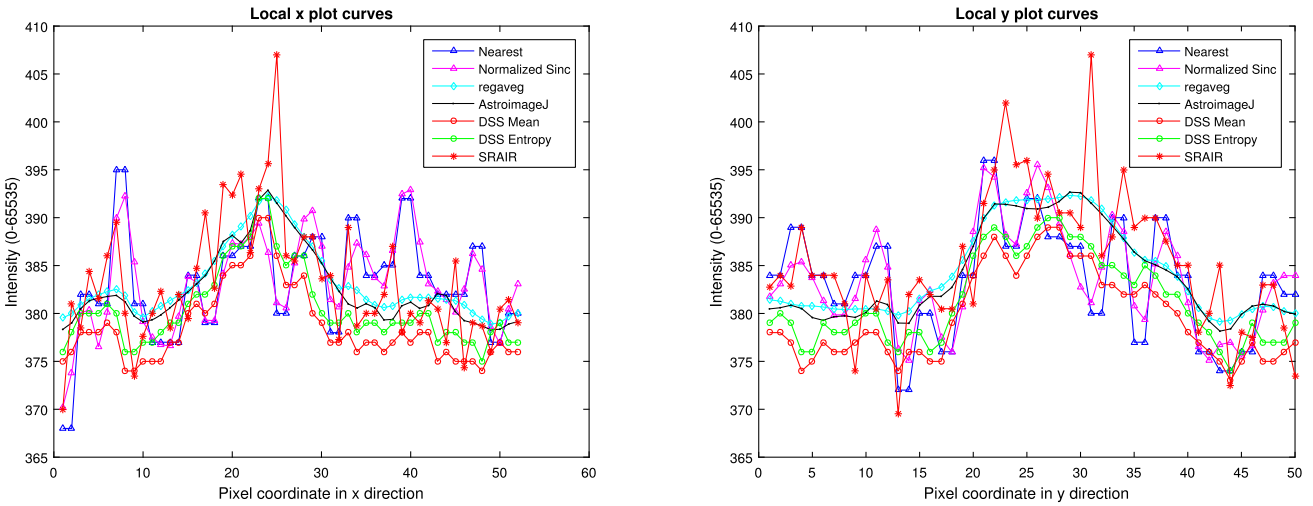

Fig. 13 Section curve in x and y directions on the intensity peak in area No. 4

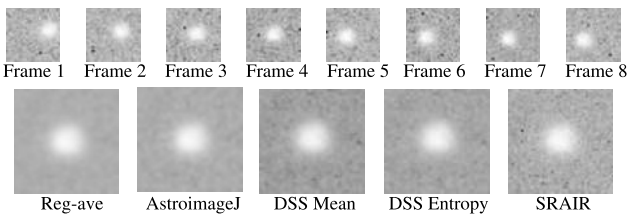

Fig. 14 Local selected image sequence of star area

discarded, because they were either too close to the image boundary, next to some high-level noise points, or influenced severely by another nearby star. For each star, a square local area sequence was selected for combination or SR reconstruction. Figure 14 shows such a selected local sequence and the outputs of the five afore-mentioned approaches.

For each reconstructed local star area, three indexes were calculated in pixels. Figures 15, 16, 17 relate these indexes to star magnitudes, among which Fig. 15 uses a relative RMS contrast (which comes from raw RMS contrast values minus the corresponding RMS values of the Reg-ave method) to render the difference distinguishable. These figures show that, in general, the SRAIR system produces the largest RMS contrast and image entropy, as well as the smallest FWHM value.

As the values of these indexes in the bright and faint star areas differ considerably, we divided the selected stars into two groups according to their magnitudes: bright stars with magnitudes 10–14 (SNR = 1240–99) and faint stars with magnitude 14.1–18 (SNR = 99 − 5).

Tables 2, 3, 4 list the mean values of these indexes for bright star areas, faint star areas, and all areas, respectively. Among the five image stacking and combination methods, the proposed SRAIR yields the largest mean values for the RMS contrast and entropy, and the smallest mean for the FWHM, whether for bright or faint stars.

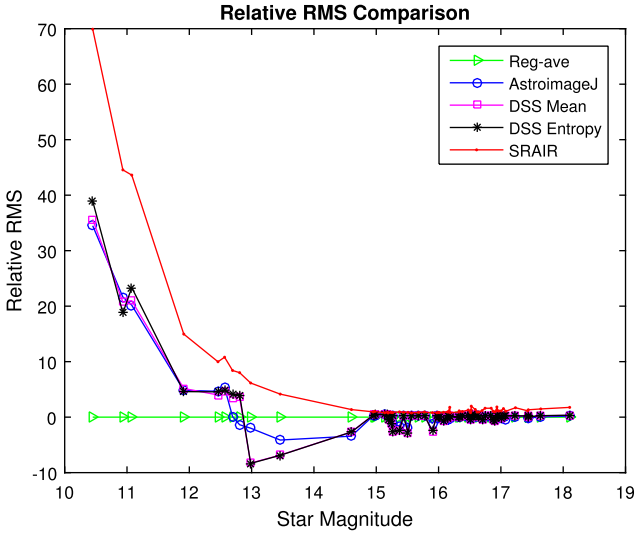

Fig. 15 Relationship between relative RMS contrast and star magnitude. To better show the differences, the relative RMS contrast is used, which means the RMS from the Reg-ave is subtracted to all corresponding RMS contrast values

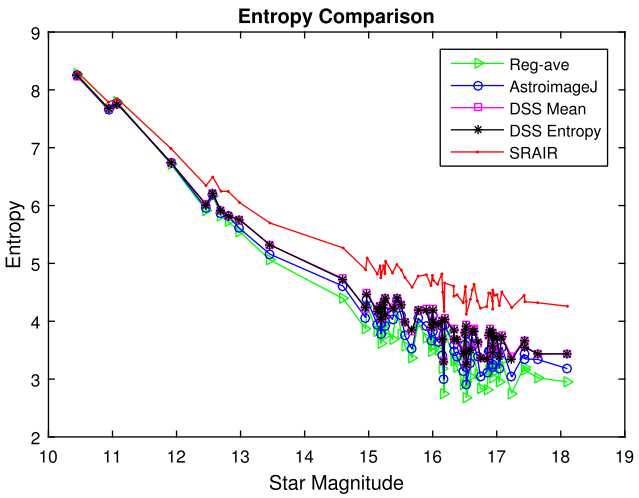

Fig. 16 Relationship between local entropy and star magnitude

According to our experiments, the proposed SRAIR solution achieves preferable resolution enhancement results, which exhibit higher star distinguishability with more details and information and less blurring.

Last, we investigated the stability of photometry and the preservation of SNR for outputs from different methods. Figure 18 relates star fluxes in various output images to their magnitudes. Curves in different colors represent different methods, among which the yellow one indicates the nearest interpolation of the reference image as a representation of the input images. The coincidences of these curves mean that stars have consistent fluxes in all output images from these methods and the input images. The flux of a star here is computed by using the method of Da Costa (1992).

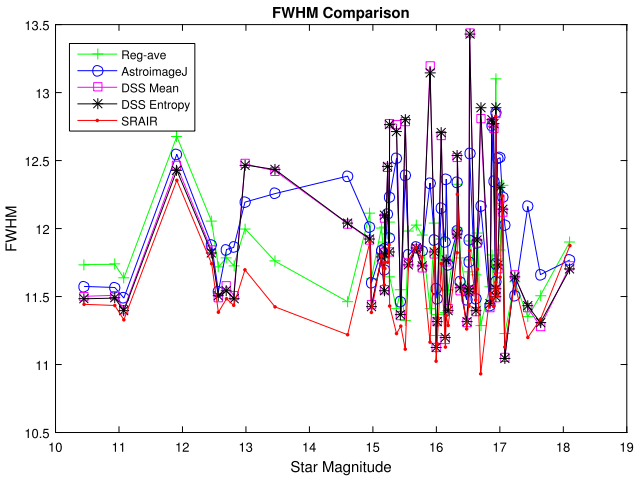

Fig. 17 Relationship between FWHM and star magnitude

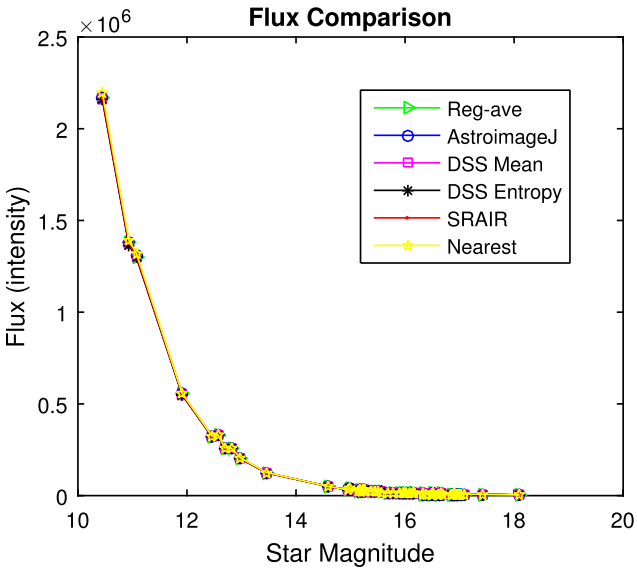

Fig. 18 Relationship between flux and star magnitude

The SNR is commonly used when referring to bright stars or faint targets. However, on the basis of the following considerations, we use star magnitudes computed from the input images themselves instead of the star SNR in this paper. On the one hand, the computation of SNR for astronomical observations requires extra information or specifications about the imaging system, while the SRAIR system is designed as a blind SR reconstruction tool for astronomical sequences independent of any instruments. On the other hand, experiments show that the observed input images have an almost uniform backgrounds after preprocessing such as flat field correction, which indicates a consistent signal extracted from noise. Therefore, star magnitudes computed by Eq. (2) in Sect. 3.1 reflect the SNR of stars quite well.

Figure 19 shows the SNR comparison of all the methods. This figure is really similar with the flux comparison in

Table 2 Local RMS contrasts (×100) of stars (in pixels)

Combining approach	Reg-ave	Astro-imageJ	DSS mean	DSS entropy	SRAIR
Bright star	0.9592	0.9720	0.9719	0.9727	**0.9929**
Faint star	0.0195	0.0192	0.0192	0.0192	**0.0211**
All	0.1686	0.1704	0.1704	0.1706	**0.1754**

Table 3 Local image entropy of stars (in pixels)

Combining approach	Reg-ave	Astro-imageJ	DSS mean	DSS entropy	SRAIR
Bright star	6.4706	6.4993	6.5464	6.5457	**6.8014**
Faint star	3.4302	3.6318	3.8597	3.8493	**4.5886**
All	3.9128	4.0870	4.2862	4.2773	**4.9398**

Table 4 FWHM of stars (in pixels)

Combining approach	Reg-ave	Astro-imageJ	DSS mean	DSS entropy	SRAIR
Bright star	11.8828	11.8752	11.8194	11.8050	**11.5727**
Faint star	11.7591	11.9912	11.9293	11.9382	**11.5618**
All	11.7808	11.9708	11.9100	11.9149	**11.5637**

Table 5 The corresponding values of star magnitude and SNR

Magnitude	10.5	11	11.5	12	12.5	13	13.5	14	14.5	15	15.5	16	16.5	17	17.5	18
SNR	1239.5	931.1	692.7	446.1	310.1	202.2	132.5	98.5	64.5	40.9	28.2	19.5	10.3	8.8	8.4	5.3

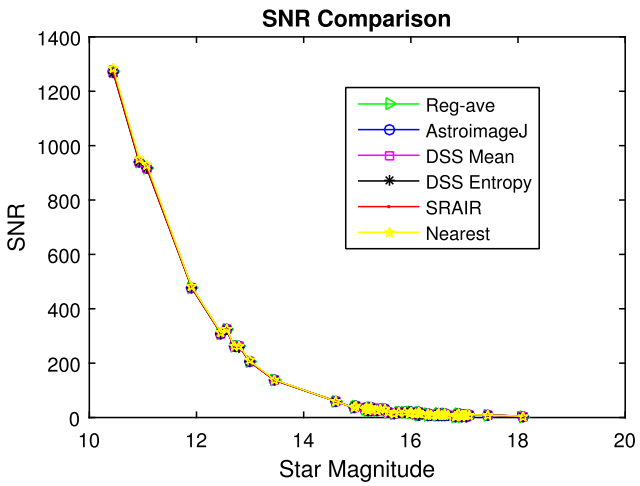

Fig. 19 Relationship between SNR and star magnitude

Fig. 18, because the SNR is computed as a function of the star flux and the star flux is related to the star magnitude directly by Eq. (2). Table 5 lists the data of star magnitudes and their corresponding SNR.

5 Conclusions

This paper proposed a general blind SR reconstruction solution for astronomical observations based on the definition of pixel reliabilities. We developed the SRAIR system and combined the flat field correction, automatic star searching and centering, iterative image registration and pixel-reliability-based SR algorithm into a complete process. In the proposed approach, beginning with high-precision star-centering techniques and sub-pixel-accuracy image registration, samples in several LR CCD frames are aligned and mapped onto a unified up-sampled grid to reconstruct an HR output image, so as to combine information from multiple observations. Experiments on actual observed frames and comparison with state-of-the-art systems verified the effectiveness of the proposed method. Richer details and sharper profiles of stars were obtained following implementation of the proposed SR reconstruction process.

The application of the proposed SR approach may provide more opportunities for new discoveries from astronomical image sequences and may also contribute to enhancing the capabilities of most spatial or ground-based telescopes. Potential applications include detecting of cosmic rays, distinguishing of dual active galactic nuclei, black-hole image reconstruction, and study of galaxies. The SRAIR system can be used as a general astronomical image resolution enhancement tool for sequences captured under a relatively stable observation conditions such as invariant imaging system, consistent atmospheric distortions, and common exposure time. Our future related research will be regarding the registration of different pixel intensity levels and the SR re-

construction for images with variable astronomical seeing, which may be caused by atmospheric turbulence.

Acknowledgements The authors would like to thank the staff working with the 1-m telescope at Yunnan Observatory for their kind help with the collection of the observation data used in this paper. The research is financially supported by the National Natural Science Foundation of China (Grant No. 11403008, U1431227, 11273014), Natural Science Foundation of Guangdong (Grant No. 2014A030313374, 2016A030313092), and the Fundamental Research Funds for the Central Universities.

References

Auer, L., Van Altena, W.: Astron. J. **83**, 531 (1978)
Bennet, F., Price, I., Rigaut, F., Copeland, M.: In: Advanced Maui Optical and Space Surveillance Technologies Conference (2016)
Cagigal, M.P., Valle, P.J., Colodro-Conde, C., Villó-Pérez, I., Pérez-Garrido, A.: Mon. Not. R. Astron. Soc. **455**(3), 2765 (2016)
Cantalupo, C., Borrill, J., Jaffe, A., Kisner, T., Stompor, R.: Astrophys. J. Suppl. Ser. **187**(1), 212 (2010)
Castellano, M., Ottaviani, D., Fontana, A., Merlin, E., Pilo, S., Falcone, M.: arXiv preprint (2015). arXiv:1501.03999
Chiu, L.-T.: Astron. J. **82**, 842 (1977)
Christou, J.C.: Publ. Astron. Soc. Pac. **103**(667), 1040 (1991)
Collins, K.A., Kielkopf, J.F., Stassun, K.G., Hessman, F.V.: Astron. J. **153**(2), 77 (2017)
Da Costa, G.: In: Astronomical CCD Observing and Reduction Techniques, vol. 23, p. 90 (1992)
Fruchter, A., Hook, R.: Publ. Astron. Soc. Pac. **114**(792), 144 (2002)
Gallaway, M.: Image Reduction and Processing, p. 119. Springer, Cham (2016)
German, A., Jenkin, M., Lespérance, Y.: In: Proceedings of the 2nd Canadian Conference on Computer and Robot Vision, 2005, p. 81. IEEE Comput. Soc., Los Alamitos (2005).
Gu, K., Zhai, G., Lin, W., Liu, M.: IEEE Trans. Cybern. **46**(1), 284 (2016)
Jarrett, T., Masci, F., Tsai, C., Petty, S., Cluver, M., Assef, R.J., Benford, D., Blain, A., Bridge, C., Donoso, E., et al.: Astron. J. **144**(2), 68 (2012)
Jarrett, T., Masci, F., Tsai, C., Petty, S., Cluver, M., Assef, R.J., Benford, D., Blain, A., Bridge, C., Donoso, E., et al.: Astron. J. **145**(1), 6 (2013)
Katsaggelos, A.K., Molina, R., Mateos, J.: Synth. Lect. Image Video Multimed. Process. **1**(1), 25 (2007)
Law, N.M., Mackay, C.D., Baldwin, J.E.: Astron. Astrophys. **446**(2), 739 (2006)
Li, Z., Peng, Q., Han, G.: Acta Astron. Sin. **50**, 340 (2009)
Neice, A.: Adv. Imaging Electron Phys. **163**, 117 (2010)
Obuchi, T., Ikeda, S., Akiyama, K., Kabashima, Y.: arXiv preprint (2016). arXiv:1611.07197
Orieux, F., Giovannelli, J.-F., Rodet, T., Abergel, A., Ayasso, H., Husson, M.: Astron. Astrophys. **539**, 38 (2012)
Park, S.C., Park, M.K., Kang, M.G.: IEEE Signal Process. Mag. **20**(3), 21 (2003)
Peli, E.: J. Opt. Soc. Am. A **7**(10), 2032 (1990)
Peng, Q., Vienne, A., Lainey, V., Noyelles, B.: Planet. Space Sci. **56**(14), 1807 (2008)
Renard, S., Thiébaut, E., Malbet, F.: Astron. Astrophys. **533**, 64 (2011)
Shannon, C.: Bell Syst. Tech. J. **27**, 379 (1948)
Stetson, P.: Astron. J. **84**, 1056 (1979)
Stone, R.C.: Astron. J. **97**, 1227 (1989)
Stone, H.S., Orchard, M.T., Chang, E.-C., Martucci, S.A.: IEEE Trans. Geosci. Remote Sens. **39**(10), 2235 (2001)
Tabur, V.: Publ. Astron. Soc. Aust. **24**(4), 189 (2007)
Thum, C.: J. Mod. Opt. **31**(2), 203 (1984)
van Altena, W.F., Auer, L.H.: In: De Jager, C., Nieuwenhuijzen, H. (eds.) Digital Image Centering, vol. I, p. 411. Springer, Dordrecht (1975)
Wang, C., Tang, D., Wang, Y., Zhao, Z., Wang, J., Pu, M., Zhang, Y., Yan, W., Gao, P., Luo, X.: Sci. Rep. **5**, 18485 (2015)